



Lisbon Atomic Database (LISA): a compilation of calculated fundamental atomic parameters

Gonalo Baptista^a, Daniel Pinheiro^b, Jorge Machado^c, Mauro Guerra^d, Pedro Amaro^e, and Jose Paulo Santos^f 

Laboratory of Instrumentation, Biomedical Engineering and Radiation Physics (LIBPhys-UNL), Department of Physics, NOVA School of Science and Technology, NOVA University of Lisbon, 2829-516 Almada, Portugal

Received 23 August 2023 / Accepted 21 December 2023 / Published online 9 February 2024
© The Author(s) 2024

Abstract. The Lisbon Atomic Database (LISA) has a dedicated mission of compiling and providing a comprehensive collection of atomic parameters for the study of the interaction of X-rays with matter. This encompassing array of parameters spans a broad spectrum, extending from the calculation of electron impact ionization cross sections (EIICS) using the Modified Relativistic Binary Encounter Bethe model (MRBEB), to pivotal data such as fluorescence and Coster–Kronig yields of atomic subshells, binding energies, and the full suite of radiative and non-radiative atomic transition parameters. Except for the EIICS values, all these parameters are obtained through ab initio calculations. These calculations are carried out using a self-consistent ab initio Multi-Configuration Dirac–Fock approach, supported by a specialized code developed by Desclaux, Indelicato, and others (MCDFGME).

1 Introduction

In the process of developing or refining an experimental method, the presence of a trustworthy and coherent theoretical model is of paramount importance. This holds immense significance throughout the entire process, ranging from the initial construction of the scientific apparatus to the subsequent interpretation and analysis of the acquired experimental data. Particularly in the context of high-precision measurements involving intricate systems, the demand for a reliable model is amplified even further. Unfortunately, the precise nature of the required data can occasionally result in its unavailability and its limited accessibility within a generic database.

As an example, the reliable characterization of nanomaterials requires techniques that often need to be adapted to the nano-scaled dimensions of the samples. The traceability of analytical methods relies on reference materials or qualified calibration samples, with spatial elemental distributions that must be very similar to the nanomaterial of interest. However, at the nanoscale, well-known reference materials are scarce or even non-existent. Thus, quantifications of the physical

properties of such nanomaterials usually need the accurate knowledge of X-ray fundamental parameters [1]. In fact, since 2008, an international initiative, whose primary goal is to obtain, either experimentally or theoretically, a consistent set of fundamental parameters (FP) that describe the interaction of X-rays with matter, was created as a joint venture of national metrology laboratories, research universities, and companies devoted to the advancement of X-ray methodologies [2]. Given the high costs of remaking all of the FP measurements with newer, more accurate techniques, the inclusion of theoretical values in the databases gathers a wide consensus. Part of the tasks of this international initiative is to perform low uncertainty experiments to be used as benchmarks for simpler and cheaper state-of-the-art calculations [3, 4]. Thus, a consistent and complete set of accurate calculations of fundamental parameters, benchmarked at certain elements of interest, is significant for the advancement of X-ray technologies.

To address this challenge, the **Lisbon Atomic Physics Database** [5], known as LISA, was established to offer accessible theoretical fundamental atomic parameters. These parameters serve as valuable resources for constructing models across a wide spectrum of physical domains linked to Atomic Physics. This extends to fields such as Plasma Physics, Astrophysics, High-Resolution X-Ray Spectroscopy, and numerous others, where these parameters play a pivotal role.

^a e-mail: g.baptista@campus.fct.unl.pt

^b e-mail: ds.pinheiro@campus.fct.unl.pt

^c e-mail: jfd.machado@fct.unl.pt

^d e-mail: mguerra@fct.unl.pt

^e e-mail: pdamaro@fct.unl.pt

^f e-mail: jps@fct.unl.pt (corresponding author)

2 Calculation methods

In this section, a concise overview of the methodology used to calculate the upcoming parameters will be provided. For a more comprehensive understanding of the calculation methods employed, readers are encouraged to refer to [6–8, 10–12].

2.1 Electron Impact Ionization Cross sections

Electron Impact Ionization Cross sections hold a large significance in the exploration and development of theoretical models in Plasma Physics. The computation of these cross sections is notably complex and extensive, owing to the multitude of involved physical processes.

Within this database, Electron Impact Ionization Cross section (EIICS) values are furnished through the utilization of modified adaptations of the semi-empirical Binary Encounter Bethe (BEB) model, as pioneered by Kim et al. [13] and latter followed by Guerra et al. [6]. These adaptations were aimed at simplifying the model's complexity and accounting for high-velocity relativistic corrections. This led to the creation of two novel models: the non-relativistic Modified BEB (MBEB) and its relativistic counterpart, the Modified Relativistic BEB (MRBEB). These models exhibit an elegant simplicity, relying only on two atomic parameters—the binding energy of ionized electrons and the effective charge Z of atomic orbitals.

Extensive calculations carried out using these two models have demonstrated their accuracy in effectively estimating Electron Impact Ionization Cross sections for K, L, and M shells.

2.2 MCDFGME calculated parameters

Central to this database's mission is the inclusion of parameters intricately linked to the atomic electronic structure and potential decay pathways. These crucial properties have been calculated using the *ab initio* self-consistent Multi-Configuration Dirac-Fock General Matrix Elements (MCDFGME) code [7, 8] (<http://kroll.lkb.upmc.fr/mcdf/>). This specialized code, a collaborative achievement by Desclaux and Indelicato, is consistently advancing through regular updates (<https://www.lkb.upmc.fr/metrologysimplesystems/mdfgme-a-general-purpose-multiconfiguration-dirac-foc-program/>).

Fundamentally, this code addresses the Dirac equation within a many-body system, adeptly tailored to a particular configuration and an assigned set of quantum numbers. This comprehensive approach encompasses the incorporation of Breit's interaction, while simultaneously accommodating the inclusion of electronic correlation and second-order Quantum Electrodynamics (QED) energetic corrections [7, 9].

2.2.1 Binding energies

The determination of binding energies for each subshell involves the application of the Dirac-Breit Hamiltonian to the single-electron wave function of the respective subshell. Following this step, the process incorporates QED energy corrections, like vacuum polarization and self-energy, which are obtained through the application of perturbation theory.

2.2.2 Radiative and non-radiative transition rates and widths

After obtaining a set of precomputed wavefunctions for both 1-hole and 2-hole systems, the subsequent step involves the computation of transition rates (denoted as R). This computation encompasses all conceivable decay paths that bridge between higher- and lower-energy configurations. This intricate calculation systematically spans across every feasible combination of two 1-hole configurations, culminating in the generation of a comprehensive spectrum of radiative transitions. Moreover, this computational process is expanded to encompass the entire array of conceivable pairings between 1-hole and 2-holes configurations, which specifically correspond to the non-radiative Auger electron emissions. Moreover, it is also possible to perform calculations of level energies and transition rates for the satellite states that arise as a consequence of Auger transitions or shake processes.

Each computed transition will yield its respective energy and rate, which in turn can be utilized to determine the transition's partial width. This width is linked to the resulting energy spread inherent to the natural broadening indicated by Heisenberg's uncertainty principle, given by $\Gamma = \hbar R$.

In the context of radiative decays, an initial 1-hole state characterized by a vacancy in the subshell indicated by the subscript i may undergo a decay into lower-energy states. This transition involves the vacancy shifting to a higher subshell, denoted by the subscript j , through the emission of electromagnetic radiation. The total radiative width, denoted as Γ_R , for the initial subshell is defined as the sum of all the partial widths associated with the possible radiative decay pathways (as outlined in Eq. (1)).

$$\Gamma_i^R = \sum_j \Gamma_{ij}^R \quad (1)$$

To calculate the subshell's non-radiative width, Γ_i^{NR} , associated with Auger transitions, a comparable procedure is employed (cf. Eq. (2)). In this case, the subscript i continues to signify the initial 1-hole state's vacancy subshell, while subscripts j and k denote the higher-up subshell vacancies corresponding to the final 2-hole state.

$$\Gamma_i^{NR} = \sum_{j \geq k} \Gamma_{ijk}^{NR} \quad (2)$$

The expression $j \geq k$ was used as not to account twice for the same Auger transition.

The total width of the subshell can now be calculated by summing the radiative and non-radiative widths:

$$\Gamma_i^T = \Gamma_i^R + \Gamma_i^{NR} \tag{3}$$

2.2.3 Fluorescence yields

By definition, a subshell’s fluorescence yield, denoted as w_i , is established as the ratio between the radiative width and the total width of that specific subshell:

$$w_i = \frac{\Gamma_i^R}{\Gamma_i^R + \Gamma_i^{NR}} \tag{4}$$

2.2.4 Coster–Kronig Auger transition yields

In the context of a Coster–Kronig Auger transition, the electron that occupies the initial state’s vacancy must originate from the same shell as the ejected electron. In this manner, for a Coster–Kronig transition to occur, the subshells denoted by j or k need to belong to the same shell as the one represented by i . A special case arises when all three subshells involved in the process belong to the same shell, a Super Coster–Kronig has occurred.

As for the Coster–Kronig subshell width:

$$\Gamma_i^{NR-CK} = \sum_{j \geq k} \Gamma_{ijk}^{NR} \cdot \mathcal{H}(\Delta_{ij} + \Delta_{ik} - 0.5) \tag{5}$$

For the Super Coster–Kronig:

$$\Gamma_i^{NR-SCK} = \sum_{j \geq k} \Gamma_{ijk}^{NR} \cdot (\Delta_{ij} \cdot \Delta_{ik}) \tag{6}$$

where \mathcal{H} represents Heaviside’s function and Δ_{ij} and Δ_{ik} denote the modified Kronecker deltas that operate on the shells i, j and k belong to.

Similarly to the previous cases, the Coster–Kronig yield, f_i , can now be computed as:

$$f_i = \frac{\Gamma_i^{NR-CK}}{\Gamma_i^R + \Gamma_i^{NR}} \tag{7}$$

2.2.5 Spectral emission parameters

While an electron can belong to a certain subshell, the different possible angular momentum couplings between the different electrons in the system lead to splittings in the energy levels. For this reason, when dealing with atomic energy levels and the consequent state transitions, the following three different sets of quantum numbers influence the energy spectrum:

- (n, l_j) —indicator of the subshell(s) of the missing electron(s)

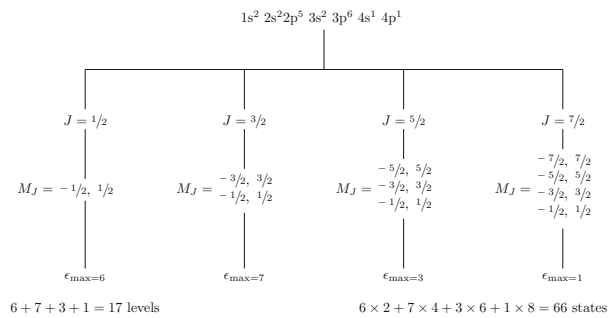


Fig. 1 Splitting of quantum numbers for a given configuration

- J —the total angular momentum of the atomic system
- ϵ —the Lagrange multiplier for the present configuration, related to how a certain combination of $(nl_j), J$ can be achieved for many coupling possibilities.

The level calculations do not take into account the presence of an external electromagnetic field; therefore, computations are only performed for the maximum J projection and a $2J + 1$ degeneracy is considered. A certain configuration can therefore have a plethora of different states associated to it, as exemplified in Fig. 1.

Emission energy The energy of a spectral line is given by the energetic difference between the atomic levels:

$$E_{ij} = E[(n, l_j)_f, J_f, \epsilon_f] - E[(n, l_j)_i, J_i, \epsilon_i] \tag{8}$$

The branching-out of the level diagram as consequence of all the different couplings will result in a very complex cascade of transitions. This way, a typical emission line is commonly composed of not only one transition, but a manifold of all the different emission lines from the complex-level structure.

Spectral intensity After performing the computation for all possible level transitions, one can now start to calculate the intensity for each radiative spectral line. For this calculation, the level and the subshell’s multiplicities need to be taken into account.

The level multiplicity is simply given by the angular momentum degeneracy: $g[(n, l_j), J, \epsilon] = 2J + 1$, and the subshell’s, g_{sub} , by the sum of all the multiplicities of every level belonging to that subshell:

$$g_{sub} \equiv g[(n, l_j)] = \sum_{J, \epsilon} g[(n, l_j), J, \epsilon] \tag{9}$$

with i and f now representing levels with quantum number sets $[(n, l_j)_i, J_i, \epsilon_i]$ and $[(n, l_j)_f, J_f, \epsilon_f]$, respectively, the expression for the intensity for each individ-

ual transition [12] is now given by:

$$I_{if} = N_i \frac{g_i}{g_{sub i}} \frac{\Gamma_{if}^R}{\sum_f \Gamma_{if}^R + \sum_{j \geq k} \Gamma_{ijk}^{NR}} \quad (10)$$

where N_i is a scaling factor related to the density of population of the initial state. For the sake of this database, all values of N_i will be that of 1, so the user is able to model their data as they please.

Transition energy width Having calculated, for each level, every possible decay path's (radiative and non-radiative) partial widths, defined as the product of reduced Planck constant (\hbar) and the rate of the transition, the sum of all these values for transitions originating from a certain initial level will yield the level's width. The true natural line width for an atomic transition can now be determined as by summing the total widths of both the initial and final levels involved:

$$\Gamma_{ij}^T = \Gamma_i^T + \Gamma_f^T \quad (11)$$

Intensity ratio For the calculation of the transition intensity ratio between two different spectral lines (e.g. the $K\alpha_1/K\alpha_2$ ratio), one must not forget that, as previously mentioned, these are mostly composed of various spectral emissions; therefore, for each transition, it is necessary to look at the configurations of the initial and final levels and decide whether or not that transition is of relevance. After this selection, the intensities of each selected spectral line should be added up and the ratio computed. It is of significant importance to remind oneself to properly use the scaling factor, bear in mind the correct utilization of the scaling factor, N_i , provided by (10). This ensures the correct computation of the desired ratio, tailored to the specifics of the experimental configuration.

Spectral line shapes While the parameters computed earlier can contribute to the computation of the natural line shape of emission, it is necessary to consider the experimental setup alongside the resolution and response functions of the radiation detector.

The natural line shape can be described by a Lorentzian distribution centered around the emission energy E_{if} , with the transition energy width, Γ_{if}^T , serving as a broadening factor, and the calculated intensity, I_{if} as a scaling parameter:

$$L \equiv L(E - E_{if}, \Gamma_{if}^T, I_{if}) = \frac{I_{if} \cdot \Gamma_{if}^T / 2\pi}{(E - E_{if})^2 + (\Gamma_{if}^T / 2)^2} \quad (12)$$

If a spectrum were to be simulated solely using this profile, similar to the one depicted in Fig. 3, its validity would be limited to emission from stationary atoms, for which the thermal distribution follows a Dirac delta function. Nevertheless, this simulation would be accurate only if there were no stochastic

elements in the interaction between radiation and the detector, as well as other components of the experimental setup, and if these interactions were entirely deterministic in nature. However, reality deviates from such ideal conditions. Hence, a new form of broadening for the spectral lines needs to be considered and incorporated. For this, a convolution of the Lorentzian profiles with a Gaussian distribution, as in Eq. (13), with a broadening parameter σ associated to the experimental resolution should be computed in order to compare the theoretical spectra with the experimental ones. This operation leads to a profile also known as the Voigt distribution. While there is no analytical expression for this distribution, due to the complexity of the operation, Eq. (14) shows how the values can be obtained from the real part of the Faddeeva function, $w(z)$.

$$G \equiv G(E, \sigma) = \frac{1}{\sigma\sqrt{2\pi}} \exp\left(-\frac{E^2}{2\sigma^2}\right) \quad (13)$$

$$\begin{aligned} V(E - E_{if}, \Gamma_{if}^T, \sigma, I_0) &= \int_{-\infty}^{\infty} L(E - E_{if} - E', \Gamma_{if}^T, I_0) \cdot G(E', \sigma) \, dE' \\ &= I_0 \frac{\Re w(z)}{\sigma\sqrt{2\pi}}, \quad z = \frac{E - E_{if} + i\Gamma_{if}^T}{\sigma\sqrt{2}} \end{aligned} \quad (14)$$

2.2.6 Maximum Shake probabilities

When an atomic system undergoes the process of ionization, due to the change of the Hamiltonian and its eigenfunction set, it can subsequently experience a shake-up or shake-off event. The likelihood of these events taking place rises with the energy of the incident beam, reaching a point of saturation. These maximum (or saturation) values can be computed with the electron wavefunctions derived from an MCDGME calculation.

Total shake To calculate the total shake probability, P_{shake} , for an electron characterized by quantum numbers $(nl_j)^*$, employing the non-adiabatic or sudden regime approximation (equated with the shake-off probability according to Krause and Carlson [10]), the initial step involves subtracting from the total probability space the likelihood of the electrons retaining the mentioned quantum numbers after the transition process. This procedure is followed by the product with the probability that every other electron with $(nl_j) \neq (nl_j)^*$ kept their quantum numbers. We have

$$P_{shake} = 1 - |\langle \psi_{i(nl_j)^*} | \psi_{f(nl_j)^*} \rangle|^{2N^*} \cdot P_{stay} - N^* P_{forb} \quad (15)$$

where

$$P_{stay} = \prod_{(nl_j) \neq (nl_j)^*} (|\langle \psi_{i(nl_j)^*} | \psi_{f(nl_j)^*} \rangle|^{2N}) \quad (16)$$

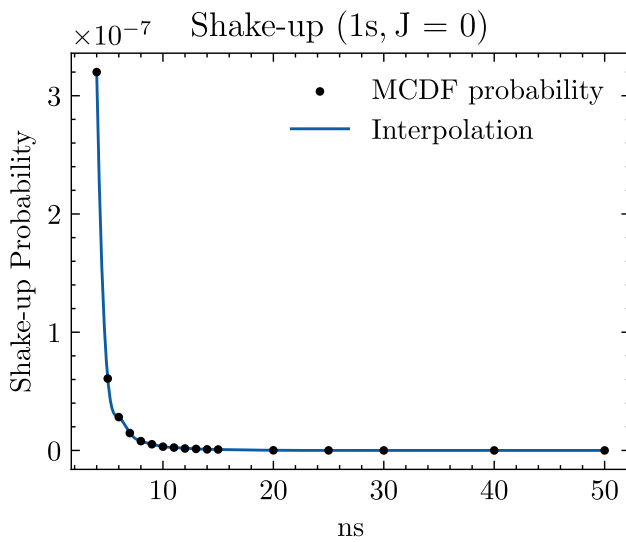


Fig. 2 Shake-up probability for an $1s \rightarrow ns$ electron excitation after a ground state Cu K shell ionization

and N_*P_{forb} considers the probability of transitions to levels forbidden by the Pauli exclusion principle, where N_* denotes the number of like electrons.

Shake-up The single shake-up probability calculation of an electron described by the wavefunction $\psi_{i(nl_j)^*}$ being excited to a state described by $\psi_{f(n'l'_j)^*}$ can be achieved by computing the squared modulus of the overlap between the initial and final wavefunctions with the desired quantum numbers for different excitations attained through M1 transitions and multiplying this value to the orbital occupation number and the probability of every other electron staying in place:

$$P_{\text{shake-up}} = N_* |\langle \psi_{i(nl_j)^*} | \psi_{f(n'l'_j)^*} \rangle|^2 \cdot P_{\text{stay}} \quad (17)$$

These values tend to diminish as the principal quantum number increases. To obtain the comprehensive shakeup probability, it is necessary to perform interpolation on the computed values, as demonstrated in Fig. 2.

Shake-off The computation of shake-off probability follows a similar approach to that of the shake-up's. However, in this case, the continuum electron's wavefunctions are used instead of the excited state's. The process involves calculating the integral of the differential probability across various energy levels of free electrons.

Alternatively, should the total shake and shake-up probabilities have already been determined, the shake-off probability can be computed in a more straightforward way. This can be achieved by simply subtracting the shake-up probability from the total shake.

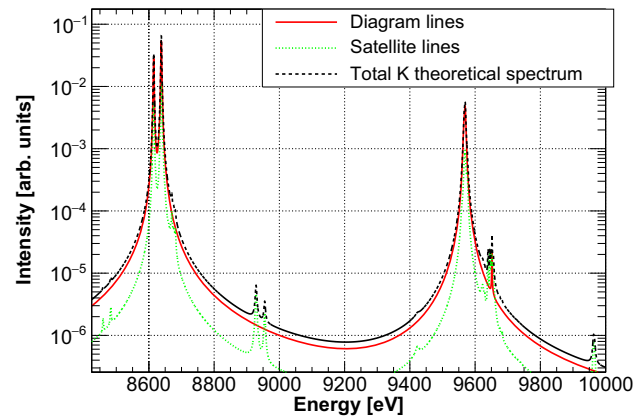


Fig. 3 Theoretical X-ray spectrum of zinc atom with a K vacancy. The red line represents the diagram lines, the green line represents the intensity of all possible satellite lines evaluated through the shake probability after a K ionization, and the black line represents the full theoretical spectrum. All quantities are calculated *ab initio* with the described formalism

Table 1 Zinc X-ray diagram transitions with a K vacancy

Line	Energy (eV)	Intensity	Width (eV)
$K - L_1$	8460.25	4.25×10^{-7}	8.64
$K - L_2$	8614.74	1.44×10^{-1}	2.42
$K - L_3$	8638.13	2.80×10^{-1}	2.46
$K - M_1$	9516.71	8.59×10^{-8}	5.16
$K - M_2$	9566.53	1.95×10^{-2}	4.63
$K - M_3$	9569.55	3.82×10^{-2}	4.55
$K - M_4$	9651.70	2.45×10^{-5}	1.66
$K - M_5$	9652.02	3.55×10^{-5}	1.66
$K - N_1$	9658.81	5.74×10^{-9}	1.66

Table 2 Electron total shake probability for each sub-shell after the creation of a K vacancy on a zinc atom

Atomic sub-shell	Total shake probability (%)
K	0.01
L_1	0.09
L_2	0.16
L_3	0.30
M_1	0.34
M_2	0.80
M_3	1.56
M_4	4.15
M_5	6.27
N_1	11.73
Total	25.40

3 About the database

LISA will provide all the aforementioned fundamental atomic parameters. Therefore, with the provided information, one can produce an ab initio theoretical spectrum with the given calculated quantities and compare it with the experimental. Frequently, the existent atomic databases only provide a given final atomic parameter, such as line energies, line widths, or even fluorescence and Coster-Kronig yields. These atomic parameters are often calculated through the computation of several electronic transitions between many energy levels due to the angular momentum coupling between the vacancy state and open outer shells, which is computationally very demanding. As an alternative, one may use the weighted average energy approach as in Ref. [14] to provide a transition energy value, yet the information of possible distortions to the line shape due to the multiplet structure of a given system cannot be inferred from this approach. The development of microcalorimeters, either transition-edge sensors (TESs) or metallic magnetic calorimeters (MMCs), with very low-energy resolution compared with the standard semiconductor detectors, made possible the experimental assessment of X-ray line shapes [15,16] for a wide energy range, which justifies the importance of the availability of all atomic transitions and related atomic parameters. Therefore, the aim of the database is to provide information of every possible transition between all 1- and 2-vacancy levels, energies, relative intensities, shake probabilities, level and line widths, and all relevant atomic parameter that will allow a user to build up a synthetic theoretical spectrum that could be compared to experiment. For instance, if we considered the zinc atom with the emission of a K bound electron to the continuum, neglecting the involved process that has produced the K vacancy ($N_i = 1$), the atom will relax with the emission of either a photon or an Auger electron. Figure 3 shows the full X-ray emission theoretical spectrum after K -ionization. While the diagram lines are plotted using the parameters of the diagram transitions of Table 1 (red line), for the width and intensity of the satellite lines it is assumed that

the fluorescence yield is similar to that of the diagram line [17,18]. Furthermore, with this approximation and with the calculated shake probabilities using the sudden approximation methodology, the satellite transitions can also be predicted from the calculated atomic parameters (green line). The solid black line in Fig. 3 depicts the full spectrum resulting from the K -shell ionization of the zinc atom. This spectrum encompasses the combined intensity of the diagram lines as well as the satellite lines arising from the shake process, whose probability is listed in Table 2.

In Table 3 we presented the calculated sub-shell fluorescence yields of zinc compared with literature. As it can be seen, the calculation of the K fluorescence yield is in agreement with the most recent experimental value and with former experiments and calculations. For the other sub-shells, the literature is scarce and there are not many experiments to compare with, for the best of our knowledge.

As all Auger transitions are also calculated for the determination of the level widths, fluorescence yields, and line intensities, in Table 4 we also present the Auger spectrum for the zinc atom with a K -hole. The intensity, as in the case of Table 1, is normalized to the yield defined by equation 4, being the Auger yield defined by $1 - w_i$.

On its present form, the database presents atomic fundamental parameters of Lithium, Neon, Magnesium, Aluminum, Silicon, Argon, Calcium, Iron, Nickel, Zinc, Germanium, Selenium, Krypton, Yttrium, Zirconium, Tin, Xenon, Barium, Lanthanum, Cerium, Neodymium, Samarium, Gadolinium, Dysprosium, Erbium, Ytterbium, Mercury, Radon, Thorium, and Oganesson, from previously computed atomic parameters from the group [12,18,26–32].

4 Conclusion

The Lisbon Atomic Database will encompass a plethora of fundamental theoretical parameters that are of great relevance for the study and development of new

Table 3 Fluorescence yield of each sub-shell for the zinc atom

Atomic sub-shell	Fluorescence Yield							
	Theoretical			Experiment				
	Ref. [19]	Ref. [20]	Ref. [21]	Ref. [22]	Ref. [23]	Ref. [24]	Ref. [25]	This work
K	0.488	0.482	0.469369	0.471(25)	0.481(7)	0.477(38)	0.495(22)	0.48148
L_1			0.0018		0.0117(18)			0.00089
L_2			0.0095					0.00373
L_3			0.012					0.00703
M_1			0.0000046		0.000108			0.00001
M_2			0.000022					0.00002
M_3			0.0					0.00003
M_4			0.00253125					0.40000
M_5			0.0					0.60000

Table 4 Zinc Auger spectrum with an initial K vacancy

Line	Energy (eV)	Intensity	Width (eV)
$K - L_1L_1$	7193.61	3.86E-02	17.50
$K - L_1L_2$	7333.57	7.65E-02	27.94
$K - L_1L_2$	7365.13	5.39E-03	20.36
$K - L_1L_3$	7376.42	1.70E-02	23.67
$K - L_1L_3$	7389.29	1.51E-02	20.30
$K - L_2L_2$	7481.58	1.49E-02	3.64
$K - L_2L_3$	7513.79	2.03E-01	3.62
$K - L_2L_3$	7524.58	1.34E-04	3.61
$K - L_3L_3$	7531.30	5.67E-03	3.62
$K - L_3L_3$	7545.77	3.37E-02	3.59
$K - L_1M_1$	8288.52	9.99E-03	55.26
$K - L_1M_1$	8289.67	5.22E-05	8.47
$K - L_1M_2$	8336.36	7.26E-03	9.74
$K - L_1M_2$	8337.32	7.30E-04	6.52
$K - L_1M_3$	8339.56	4.68E-03	8.30
$K - L_1M_3$	8340.60	2.09E-03	6.68
$K - L_1M_5$	8422.19	4.16E-05	8.86
$K - L_1M_4$	8424.77	1.51E-04	8.81
$K - L_1M_4$	8424.98	2.29E-04	8.82
$K - L_1M_5$	8425.23	3.02E-04	8.80
$K - L_2M_1$	8440.80	4.41E-03	2.51
$K - L_2M_1$	8441.77	5.44E-04	2.48
$K - L_1N_1$	8441.88	6.08E-04	11.34
$K - L_1N_1$	8442.10	4.03E-06	8.67
$K - L_3M_3$	8463.44	6.18E-03	2.53
$K - L_3M_3$	8465.20	1.40E-03	2.47
$K - L_2M_2$	8492.83	2.36E-03	4.75
$K - L_2M_3$	8492.97	2.61E-02	2.52
$K - L_2M_3$	8494.05	8.06E-06	2.53
$K - L_2M_2$	8494.36	2.45E-05	2.48
$K - L_3M_2$	8513.92	2.56E-02	2.36
$K - L_3M_2$	8514.44	6.66E-05	2.51
$K - L_3M_2$	8515.23	7.98E-04	2.67
$K - L_3M_3$	8518.18	2.92E-03	4.11
$K - L_3M_3$	8520.76	7.35E-05	2.48
$K - L_3M_3$	8521.01	1.18E-05	2.48
$K - L_2M_4$	8577.06	1.40E-05	2.64
$K - L_2M_5$	8578.19	1.71E-03	2.64
$K - L_2M_5$	8579.00	2.72E-05	2.52
$K - L_2M_4$	8580.52	3.70E-04	2.10
$K - L_2N_1$	8596.38	2.38E-04	2.47
$K - L_2N_1$	8596.45	3.20E-05	2.46
$K - L_3M_5$	8599.67	1.73E-05	2.61
$K - L_3M_5$	8600.03	1.87E-03	2.75
$K - L_3M_4$	8600.96	9.29E-06	2.42
$K - L_3M_4$	8601.37	1.84E-05	2.54
$K - L_3M_4$	8602.02	5.27E-05	2.59
$K - L_3M_4$	8603.10	3.18E-04	2.44
$K - L_3M_5$	8604.22	9.00E-05	2.25
$K - L_3M_5$	8604.41	8.04E-04	2.02
$K - L_3N_1$	8619.71	3.95E-04	2.45
$K - L_3N_1$	8619.83	8.15E-05	2.45
$K - M_1M_1$	9344.27	6.51E-04	6.00
$K - M_1M_3$	9388.43	1.18E-03	24.85
$K - M_1M_2$	9402.32	7.49E-05	13.66
$K - M_1M_2$	9403.47	1.73E-04	13.38
$K - M_1M_3$	9405.40	1.98E-04	12.75
$K - M_2M_2$	9440.67	2.71E-04	7.77
$K - M_2M_3$	9447.56	2.75E-03	6.77

Table 4 continued

Line	Energy (eV)	Intensity	Width (eV)
$K - M_3M_3$	9451.03	2.27E-05	7.15
$K - M_2M_3$	9451.14	2.19E-06	7.16
$K - M_3M_3$	9453.62	1.81E-04	6.95
$K - M_1M_5$	9478.26	2.19E-06	5.23
$K - M_1M_4$	9484.06	1.60E-05	5.32
$K - M_1M_4$	9484.21	2.42E-05	5.34
$K - M_1M_5$	9484.43	3.18E-05	5.36
$K - M_1N_1$	9498.57	7.92E-05	4.14
$K - M_1N_1$	9498.80	6.57E-09	5.06
$K - M_2M_5$	9524.36	2.95E-04	7.67
$K - M_2M_4$	9525.46	1.44E-06	5.63
$K - M_2M_5$	9532.55	1.19E-06	5.29
$K - M_2M_4$	9533.07	2.46E-07	5.61
$K - M_3M_5$	9534.19	3.89E-06	5.67
$K - M_3M_4$	9534.85	3.27E-06	4.66
$K - M_3M_4$	9535.36	2.18E-06	4.33
$K - M_3M_4$	9535.44	8.68E-07	4.18
$K - M_2M_4$	9538.35	2.84E-05	3.12
$K - M_3M_4$	9540.34	5.89E-05	2.85
$K - M_3M_5$	9540.50	1.53E-05	3.18
$K - M_3M_5$	9541.70	7.18E-05	2.77
$K - M_2N_1$	9548.10	3.58E-05	4.74
$K - M_2N_1$	9548.30	4.42E-06	4.56
$K - M_3N_1$	9550.99	4.56E-05	4.54
$K - M_3N_1$	9551.33	1.15E-05	4.35
$K - M_5M_5$	9610.82	3.25E-08	1.66
$K - M_4M_5$	9616.61	1.33E-05	1.66
$K - M_4M_4$	9617.37	8.88E-11	1.66
$K - M_4M_5$	9617.42	2.70E-10	1.66
$K - M_4M_5$	9617.49	2.22E-08	1.66
$K - M_5M_5$	9618.08	1.28E-07	1.66
$K - M_4M_4$	9620.27	7.60E-10	1.66
$K - M_4M_5$	9620.46	3.62E-09	1.66
$K - M_5M_5$	9620.76	1.51E-08	1.66
$K - M_4N_1$	9633.17	2.37E-07	1.66
$K - M_4N_1$	9633.57	9.48E-07	1.66
$K - M_5N_1$	9633.75	1.32E-06	1.66
$K - M_5N_1$	9633.90	1.89E-06	1.66
$K - N_1N_1$	9641.96	2.41E-06	1.66

exploratory probes for physical systems in the areas related to atomic physics. These parameters range from Electron Impact Ionization Cross sections, calculated through simplistic but reliable semi-empirical models, to the many atomic parameters computed by employing an ab initio self-consistent method of solving the many-body Dirac equation.

Acknowledgements We acknowledge the support of the following grants: FCT—Fundação para a Ciência e a Tecnologia (Portugal) through national funds in the frame of projects UID/04559/2020 (LIBPhys). This work was also funded through the project PTDC/FIS-AQM/31969/2017, “Ultra-high-accuracy X-ray spectroscopy of transition metal oxides and rare earths.” D.P. acknowledges support from FCT, under Contract No 2022.13412.BD. We would also like to thank and acknowledge Paul Indelicato for providing a recent version of the MCDFGME code (2019 version),

which was used for the calculation of the data present in this work.

Author contributions

All authors contributed equally in the development and execution of the present study.

Funding Information Open access funding provided by FCT—FCCN (b-on).

Data Availability Statement This manuscript has associated data in a data repository. [Authors's comment: The data generated in this current study are available in the manuscript and are/will be deposited on the database url (<https://lisa.libphys.pt/>). In addition, all generated data are available from the corresponding author on reasonable request.]

Open Access This article is licensed under a Creative Commons Attribution 4.0 International License, which permits use, sharing, adaptation, distribution and reproduction in any medium or format, as long as you give appropriate credit to the original author(s) and the source, provide a link to the Creative Commons licence, and indicate if changes were made. The images or other third party material in this article are included in the article's Creative Commons licence, unless indicated otherwise in a credit line to the material. If material is not included in the article's Creative Commons licence and your intended use is not permitted by statutory regulation or exceeds the permitted use, you will need to obtain permission directly from the copyright holder. To view a copy of this licence, visit <http://creativecommons.org/licenses/by/4.0/>.

References

1. B. Beckhoff, Traceable characterization of nanomaterials by x-ray spectrometry using calibrated instrumentation. *Nanomaterials* **12**(13), 2255 (2022)
2. M. Guerra, M.-C. Lépy, J.P. Santos, B. Beckhoff, Special issue editorial - x-ray fundamental parameters: bridging science and technology. *Radiat. Phys. Chem.* **212**, 111097 (2023)
3. M. Guerra, J.M. Sampaio, T.I. Madeira, F. Parente, P. Indelicato, J.P. Marques, J.P. Santos, J. Hozowska, J.C. Dousse, L. Loperetti, F. Zeeshan, M. Muller, R. Unterumsberger, B. Beckhoff, Theoretical and experimental determination of *L*-shell decay rates, line widths, and fluorescence yields in Ge. *Phys. Rev. A* **92**(2), 022507 (2015)
4. M. Guerra, J.M. Sampaio, F. Parente, P. Indelicato, P. Hönicke, M. Müller, B. Beckhoff, J.P. Marques, J.P. Santos, Theoretical and experimental determination of *k*- and *l*-shell x-ray relaxation parameters in Ni. *Phys. Rev. A* **97**(4), 042501 (2018)
5. Lisbon Atomic Database. <https://lisa.libphys.pt/>
6. M. Guerra, F. Parente, P. Indelicato, J.P. Santos, Modified binary encounter Bethe model for electron-impact ionization. *Int. J. Mass Spectrom.* **313**, 1–7 (2012). <https://doi.org/10.1016/j.ijms.2011.12.003>
7. J.P. Desclaux, A multiconfiguration relativistic Dirac-Fock program. *Comput. Phys. Commun.* **9**(1), 31–45 (1975). [https://doi.org/10.1016/0010-4655\(75\)90054-5](https://doi.org/10.1016/0010-4655(75)90054-5)
8. P. Indelicato, J.P. Desclaux, Multiconfiguration Dirac-Fock calculations of transition energies with QED corrections in three-electron ions. *Phys. Rev. A* **42**, 5139–5149 (1990). <https://doi.org/10.1103/PhysRevA.42.5139>
9. O. Gorcex, P. Indelicato, J.P. Desclaux, *J. Phys. B: At. Mol. Opt. Phys.* **20**, 639 (1987). <https://doi.org/10.1088/0022-3700/20/4/006>
10. M.O. Krause, T.A. Carlson, Vacancy cascade in the reorganization of krypton ionized in an inner shell. *Phys. Rev.* **158**, 18–24 (1967). <https://doi.org/10.1103/PhysRev.158.18>
11. H.A. Melia, C.T. Chantler, Characteristic X-ray Spectroscopy
12. M. Guerra, J. Sampaio, G. Vília, C. Godinho, D. Pinheiro, P. Amaro, J. Marques, J. Machado, P. Indelicato, F. Parente, J. Santos, Fundamental parameters related to selenium k_{α} and k_{β} emission x-ray spectra. *Atoms* **9**, 8 (2021). <https://doi.org/10.3390/atoms9010008>
13. Y.-K. Kim, M.E. Rudd, Binary-encounter-dipole model for electron-impact ionization. *Phys. Rev. A* **50**(5), 3954 (1994)
14. R.D. Deslattes, E.G. Kessler, P. Indelicato, L. de Billy, E. Lindroth, J. Anton, X-ray transition energies: new approach to a comprehensive evaluation. *Rev. Mod. Phys.* **75**, 35–99 (2003). <https://doi.org/10.1103/RevModPhys.75.35>
15. J.W. Fowler, B.K. Alpert, D.A. Bennett, W.B. Doriese, J.D. Gard, G.C. Hilton, L.T. Hudson, Y.-I. Joe, K.M. Morgan, G.C. O'Neil, C.D. Reintsema, D.R. Schmidt, D.S. Swetz, C.I. Szabo, J.N. Ullom, A reassessment of absolute energies of the x-ray *l* lines of lanthanide metals. *Metrologia* **54**(4), 494 (2017). <https://doi.org/10.1088/1681-7575/aa722f>
16. C. Pies, S. Schäfer, S. Heuser, S. Kempf, A. Pabinger, J.-P. Porst, P. Ranitsch, N. Foerster, D. Hengstler, A. Kampkötter et al., MaXs: microcalorimeter arrays for high-resolution x-ray spectroscopy at GSI/FAIR. *J. Low Temp. Phys.* **167**, 269–279 (2012)
17. J.P. Marques, J.M. Sampaio, J.P. Santos, P. Indelicato, F. Parente, Theoretical fluorescence yields and widths of the *k* shell and the *l* subshells, for the Ne, Ar, and Kr isoelectronic sequences. *X-Ray Spectrom.* **49**(1), 69–73 (2020)
18. D. Pinheiro, A. Fernandes, C. Godinho, J. Machado, G. Baptista, F. Grilo, L. Sustelo, J.M. Sampaio, P. Amaro, R.G. Leitão, J.P. Marques, F. Parente, P. Indelicato, M. de Avillez, J.P. Santos, M. Guerra, *K*- and *l*-shell theoretical fluorescence yields for the Fe isonuclear sequence. *Radiat. Phys. Chem.* **203**, 110594 (2023). <https://doi.org/10.1016/j.radphyschem.2022.110594>
19. M.H. Chen, B. Crasemann, H. Mark, Relativistic *k*-shell Auger rates, level widths, and fluorescence yields. *Phys. Rev. A* **21**(2), 436 (1980)
20. V.O. Kostroun, M.H. Chen, B. Crasemann, Atomic radiation transition probabilities to the *1s* state and theoretical *k*-shell fluorescence yields. *Phys. Rev. A* **3**(2), 533 (1971)
21. T. Schoonjans, A. Brunetti, B. Golosio, M.S. del Rio, V.A. Solé, C. Ferrero, L. Vincze, The xraylib library for

- x-ray-matter interactions. Recent developments. Spectrochim. Acta, Part B **66**, 776–784 (2011). <https://doi.org/10.1016/j.sab.2011.09.011>
22. J. Pious, K. Balakrishna, N. Lingappa, K. Siddappa, Total k fluorescence yields for Fe, Cu, Zn, Ge and Mo. J. Phys. B: At. Mol. Opt. Phys. **25**(6), 1155 (1992)
 23. J.H. Hubbell, P.N. Trehan, N. Singh, B. Chand, D. Mehta, M.L. Garg, R.R. Garg, S. Singh, S. Puri, A review, bibliography, and tabulation of *K*, *I* and higher atomic shell x-ray fluorescence yields. J. Phys. Chem. Ref. Data **23**, 339–364 (1994). <https://doi.org/10.1063/1.555955>
 24. I. Han, M. Şahin, L. Demir, Y. Şahin, Measurement of k x-ray fluorescence cross-sections, fluorescence yields and intensity ratios for some elements in the atomic range $22 \leq z \leq 68$. Appl. Radiat. Isot. **65**(6), 669–675 (2007)
 25. Y. Ménesguen, M.-C. Lépy, Mass attenuation coefficients in the range $3.8 \leq e \leq 11$ keV, k fluorescence yield and k_{β}/k_{α} relative x-ray emission rate for Ti, V, Fe, Co, Ni, Cu and Zn measured with a tunable monochromatic x-ray source. Nucl. Instrum. Methods Phys. Res., Sect. B **268**(16), 2477–2486 (2010). <https://doi.org/10.1016/j.nimb.2010.05.044>
 26. J.M. Sampaio, T.I. Madeira, M. Guerra, F. Parente, J.P. Santos, P. Indelicato, J.P. Marques, Dirac-Fock calculations of *k*-, *l*-, and *m*-shell fluorescence and Coster-Kronig yields for Ne, Ar, Ar, Xe, Rn, and Uuo. Phys. Rev. A **91**, 052507 (2015). <https://doi.org/10.1103/PhysRevA.91.052507>
 27. J.P. Marques, J.M. Sampaio, J.P. Santos, P. Indelicato, F. Parente, Theoretical fluorescence yields and widths of the k shell and the l subshells, for the Ne, Ar, and Kr isoelectronic sequences. X-Ray Spectrom. **49**(1), 69–73 (2020). <https://doi.org/10.1002/xrs.3056>
 28. Y. Ménesguen, M.-C. Lépy, Y. Ito, M. Yamashita, S. Fukushima, T. Tochio, M. Polasik, K. Ślabkowska, P. Indelicato, J. Gomilsek et al., Structure of single kl0-, double kl1-, and triple kl2- ionization in Mg, Al, and Si targets induced by photons, and their absorption spectra. Radiat. Phys. Chem. **194**, 110048 (2022)
 29. M. Guerra, J.M. Sampaio, T.I. Madeira, F. Parente, P. Indelicato, J.P. Marques, J.P. Santos, J. Horszowska, J.-C. Dousse, L. Loperetti, F. Zeeshan, M. Müller, R. Unterumsberger, B. Beckhoff, Theoretical and experimental determination of *l*-shell decay rates, line widths, and fluorescence yields in Ge. Phys. Rev. A **92**, 022507 (2015). <https://doi.org/10.1103/PhysRevA.92.022507>
 30. Y. Ito, T. Tochio, M. Yamashita, S. Fukushima, A.M. Vlaicu, J.P. Marques, J.M. Sampaio, M. Guerra, J.P. Santos, L. Syrocki, K. Ślabkowska, E. Węder, M. Polasik, J. Rzakiewicz, P. Indelicato, Y. Ménesguen, M.-C. Lépy, F. Parente, Structure of $k\alpha_{1,2}$ - and $k\beta_{1,3}$ -emission X-ray spectra for Se, Y, and Zr. Phys. Rev. A **102**, 052820 (2020). <https://doi.org/10.1103/PhysRevA.102.052820>
 31. T.I. Madeira, J.M. Sampaio, M. Guerra, F. Parente, P. Indelicato, J.P. Santos, J.P. Marques, Relativistic calculation of *k*-, *l*- and *m*-shell x-ray fluorescence yields for Ba. Phys. Scr. **90**(5), 054009 (2015). <https://doi.org/10.1088/0031-8949/90/5/054009>
 32. J.P. Marques, M.C. Martins, A.M. Costa, P. Indelicato, F. Parente, J.P. Santos, Theoretical determination of k x-ray transition energy and probability values for highly charged (he- through b-like) Nd, Sm, Gd, Dy, Er, and Yb ions. Radiat. Phys. Chem. **154**, 17–20 (2019). <https://doi.org/10.1016/j.radphyschem.2018.02.003>